Modelling coastal wave trains and wave breaking

A. Duran, Gaël Loïc Richard

Modelling coastal wave trains and wave breaking

A. Duran[†] and G. L. Richard[⋆]

[†]Institut Camille Jordan, CNRS UMR 5208, Université Claude Bernard Lyon 1, 69100 Villeurbanne, France
[⋆]Univ. Grenoble Alpes, INRAE, UR ETNA, 38000 Grenoble, France

Abstract

The model of coastal waves based on the depth-averaging of the large eddy simulation equations (Kazakova & Richard 2019) is extended to the case of regular and irregular wave trains. To take into account a stronger turbulence, the third moment of the horizontal velocity is modelled with a gradient-diffusion hypothesis. The effect of this new diffusive term is to smooth and regularize the solutions. An asymptotically equivalent model including the improvement of the dispersive properties is solved with a Discontinuous Galerkin numerical scheme. The model has a low sensitivity to the space discretization parameters. Several classical test cases of wave trains are used to validate the model. In the shoaling zone, the model is similar to the Serre-Green-Naghdi equations but the inclusion of a variable called enstrophy to take into account the large-scale turbulence and the non-uniformity of the mean velocity improves the predictive ability in the inner surf zone. In particular, the turbulent energy of the model is dissipated within one wave cycle and is transported shoreward in the case of waves with a long period whereas, in the case of short periods, it is mostly transported seaward because its dissipation is far from being complete within one period. The case of an irregular wave train propagating over a submerged bar is simulated without any breaking criterion. This benchmark test case validates further the model's ability in predicting the nonlinear effects due to shoaling, breaking, propagation in a shallow horizontal part and in a deeper region.

1 Introduction

Modelling accurately coastal waves is of high importance for applications in coastal erosion and morphodynamics or for the prediction and prevention of extreme events such as great storms. For practical problems the size of the computation domain and the duration of the phenomena to be simulated are large and the computation time is an issue. This motivates the use of phase-averaged models which use a statistical description to calculate the evolution of the wave spectrum. However thanks to advances in computer performance, numerical schemes and parallel computing the phase-resolving models become more and more competitive. In these models the sea surface is resolved which necessitates a finer grid. A higher accuracy is expected but at the cost of a greater computation time.

The phase-resolving models include the non-hydrostatic approach where the Reynolds-averaged Navier-Stokes equations are solved while the non-hydrostatic part of the pressure is calculated by solving an elliptic Poisson equation [50, 37, 14]. Considerable efforts have reduced the vertical resolution needed to reproduce accurately wave breaking, from a high value of 10-20 layers to a few layers either by using a breaking criterion removing locally the non-hydrostatic part of the pressure [49] or by a superior numerical treatment using terrain and surface-following σ-coordinates [15]. These improvements lead to a significantly reduced computational cost.

In the other phase-resolving models, traditionally called Boussinesq-type models, the equations of fluid dynamics are averaged over the depth. The non-hydrostatic part of the pressure is evaluated from the depth and its derivatives which induces third-order derivatives in the model and an elliptic step in the numerical resolution. Reviews on Boussinesq-type models can be found in [8] and [28].

When propagating shoreward the waves steepen in the shoaling zone where the dispersive effects are dominant. Strictly speaking the Boussinesq equations [5], [42] are derived with a weak nonlinearity hypothesis (the wave amplitude is much smaller than the water depth) which entails some discrepancies in shallow water areas. Fully nonlinear equations were first derived by [48] in the one-dimensional (1D) case and extended in the two-dimensional (2D) case by [20] and [21] and are called in this paper the Serre-Green-Naghdi equations. Fully nonlinear models are more accurate than the Boussinesq equations, in particular in the final stages of coastal waves propagation where the wave amplitude is no longer small in comparison to the depth [62, 2, 30], but they are still weakly dispersive because of the shallow water assumption (see for example [28]) which implies that their validity is restricted to small depths. Various techniques were proposed to improve the dispersive

properties of these equations and thus to increase their validity domain. In particular [40] and [62] considered the velocity at an arbitrary depth instead of the depth-averaged velocity and [4], [31] and [9] derived an asymptotically equivalent system of equations.

Wave breaking and breakers propagation in the surf zone require to model dissipative effects. This was achieved by different approaches. The roller models are based on the concept of surface roller [51] viewed as a volume of water carried by the wave at the wave velocity [47], [38]. This method leads to several developments in particular with the inclusion of the vorticity in the model [59], [7], [39], [61] or through diffusive-type terms on both the mass and momentum equations [12]. This approach requires to calibrate several parameters notably for the breaking criterion and the determination of the roller geometry.

Another strategy is to model turbulence effects in breaking waves by an eddy viscosity [22], [63], [26]. In some models an equation for the turbulent kinetic energy is solved to calculate the eddy viscosity [41], [29], [64], [25]. A turbulent viscosity approach assumes a local balance between production and dissipation and an isotropic turbulence.

The hybrid models with a switching method are another way to take into account the dissipative effects [4], [58], [57], [24], [18], [17]. By removing the dispersive terms, the Serre-Green-Naghdi equations reduce to the Saint-Venant equations which, being hyperbolic, produce discontinuities in finite time which dissipate energy. A breaking criterion is needed to determine when the dispersive terms should be switched off and a breaking termination criterion determines when they should be switched on. This method suffers from numerical problems, in particular mesh grid sensitivity and non-physical oscillations [18], [25].

A new approach based on depth-averaging the large-eddy simulation (LES) equations was proposed by [23] in the 1D-case and extended to the 2D-case by [46], in both cases mostly for solitary waves. The large scale turbulence is explicitly resolved in a depth-averaged sense with its anisotropic properties while the small scale turbulence is modelled through a turbulent viscosity hypothesis. While there is some similarity with the eddy-viscosity strategy because of the introduction of an eddy viscosity for the small-scale turbulence, the originality of this approach lies in the anisotropic tensor modelling the large-scale turbulence which satisfies a tensor equation. There is thus no need to assume neither an approximate balance between the production and the dissipation of turbulent kinetic energy nor an isotropic turbulence, which is not always satisfied in the large scales. The resulting equations have the special hyperbolic structure of [53] with additional source terms. The goal of the present paper is to validate this approach in the more

general case of periodic and random wave trains with a special attention to the turbulence dynamics. The dynamics of surf-zone turbulence was studied experimentally by [54, 55, 56] who found that the turbulent kinetic energy is transported seaward under a spilling breaker whereas it is transported landward and dissipated within one wave cycle in the case of a plunging breaker. It is interesting to see if the depth-averaged LES approach predicts a similar behaviour.

In §2 the equations of the model of [23] are extended to the case of a stronger turbulence which requires modelling the third moment of the horizontal velocity distribution in the vertical direction. In §3 the numerical scheme is presented together with the treatment of wave breaking. In §4 the model is validated by numerical simulations of experiments on wave trains obtained by [13], [54] and [3].

2 Equations of the model

2.1 Depth-averaging procedure

The main idea of the derivation of the model equations is to average over the depth the LES equations. The details are given in [23] and only the main points and the differences from the original derivation are given here. Only two-dimensional flows are considered here which leads to a 1D-model. Details on the derivation of the 2D-model are given in [46]. Starting from the Navier-Stokes equations of incompressible fluids with a density ρ and a kinematic viscosity ν, a filtering operation decomposes the velocity field $\boldsymbol{v}$ into a filtered component $\overline{\boldsymbol{v}}$ and a residual component $\boldsymbol{v^r}$ i.e. $\boldsymbol{v} = \overline{\boldsymbol{v}} + \boldsymbol{v^r}$. The cutoff frequency is in the inertial subrange so that the filtered field includes the energy-containing motions. The residual stress tensor is modelled with a turbulent viscosity hypothesis. Contrary to the usual LES approach, the eddy viscosity of the residual motions, denoted by $\nu_T(x,t)$, is not modelled by the Smagorinsky closure but is supposed to be uniform over the depth i.e. independent of z. This simplification is sufficient for a depth-averaged model. Another important result is the equality of the dissipation of the mean residual kinetic energy and its rate of production ([32]).

The notations are given in Figure 1. We denote by g the gravity acceleration, h the total water depth, h_0 the still water depth, b the elevation of the bottom topography over a horizontal datum and $Z = h + b$. Denoting by L the wavelength or the order of magnitude of a horizontal length and by h_0^* a reference value of the still water depth, the equations are derived with an

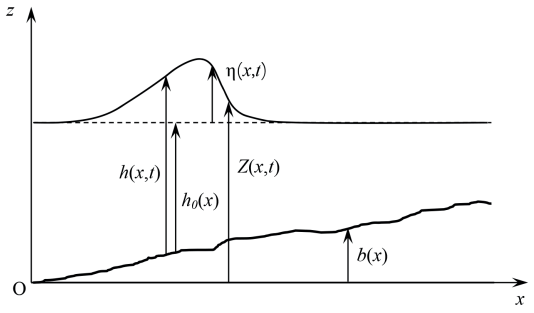

Figure 1: Notations used in the text.

asymptotic method based on the existence of the small parameter

$$\mu = \frac{h_0^*}{L} \ll 1 \tag{1}$$

of the shallow water assumption which is also responsible for the weakly dispersive properties of the equations. The Reynolds number is high so that all terms due to the molecular viscosity are negligible. As in theoretical or experimental works [52], [3], [13], [1], [64] the eddy viscosity is supposed to be of $O(\mu)$ which means that a dimensionless eddy viscosity writes

$$\tilde{\nu}_T = \frac{\nu_T}{\mu h_0^* \sqrt{g h_0^*}}. \tag{2}$$

Note however that the eddy viscosity is here relative only to the small-scale turbulence.

The averaged value of any quantity A over the depth is defined as

$$\langle A \rangle = \frac{1}{h} \int_b^{h+b} A \, \mathrm{d}z. \tag{3}$$

For the depth-averaging procedure the horizontal filtered velocity is decomposed as

$$\overline{u}(x,z,t) = U(x,t) + u'(x,z,t) \tag{4}$$

where U is the averaged value of $\overline{u}$ over the depth and u' the deviation of the filtered velocity to this average value. This deviation includes the large-scale turbulence and the depth variations of the mean (non turbulent) velocity. The flow is supposed to be weakly turbulent and weakly sheared as in [53], [45] and [10]. This means that

$$u' = O(\mu^\beta) \tag{5}$$

where $\beta > 0$. The averaging of the momentum equation in the Ox direction gives a term $\langle u^2 \rangle$ in the flux. The dimensionless filtered horizontal velocity is defined by $\tilde{u} = \overline{u}/\sqrt{gh_0^*}$. Since by definition $\langle u' \rangle = 0$, $\langle \tilde{u}^2 \rangle = \tilde{U}^2 + \mu^{2\beta} \langle \tilde{u}'^2 \rangle$. The second central moment is written with the help of the quantity

$$\varphi = \frac{1}{h^3} \int_b^{h+b} u'^2 \, \mathrm{d}z = \frac{\langle u'^2 \rangle}{h^2} \tag{6}$$

which has the same dimension as the square of a vorticity and is called enstrophy. Note that in the study of turbulent flows the enstrophy has other definitions.

Because the enstrophy is the third variable of the model, the two other ones being the fluid depth h and the average velocity U, a third equation must be derived to close the system beside the averaged mass and momentum equations. This equation can be obtained by averaging over the depth the balance equation for the kinetic energy of the filtered motions. The enstrophy appears also in the energy of the model. Moreover in the energy flux it appears the third moment of the filtered velocity which can be written in dimensionless form, with $\tilde{h} = h/h_0^*$ and $\tilde{\varphi} = h_0^* \varphi / g$, $\langle \tilde{u}^3 \rangle = \tilde{U}^3 + 3\mu^{2\beta} \tilde{h}^2 \tilde{U} \tilde{\varphi} + \mu^{3\beta} \langle \tilde{u}'^3 \rangle$. The third central moment is of $O(\mu^{3\beta})$. [10] and [23] took $\beta = 1$. The leading dispersive and viscous terms are of $O(\mu^2)$ and all terms of $O(\mu^3)$ are neglected. By taking $\beta = 1$ the third central moment can be consistently neglected. In this paper we take

$$0 < \beta < 1 \tag{7}$$

so that the turbulence can be stronger and that $\langle u'^3 \rangle$ must be consistently kept in the model. This implies that either an equation for $\langle u'^3 \rangle$ must be provided, as in [10], or that $\langle u'^3 \rangle$ must be modelled. Since highly turbulent flows can be modelled with the weak turbulence or weak shear approximation ([44], [19]) it is expected that the influence of $\langle u'^3 \rangle$ is small. The derivation of an equation for this quantity would greatly complicate the model for very little benefit. We choose instead to model this quantity with a gradient-diffusion hypothesis by analogy with the study of turbulent flows.

The enstrophy equation can be derived from the depth-averaged mass, momentum and energy equations. Because the enstrophy equation is much simpler than the energy equation and since the viscous terms prevent discontinuities from arising, the final system which is solved numerically is composed of the mass, momentum and enstrophy equations. The enstrophy equation can be written

$$\frac{\partial h\varphi}{\partial t} + \frac{\partial hU\varphi}{\partial x} = \frac{8\nu_T}{h} \left(\frac{\partial U}{\partial x} \right)^2 - \frac{2}{h} \langle \varepsilon \rangle - \frac{1}{h^2} \frac{\partial}{\partial x} \left(h \left\langle u'^3 \right\rangle \right). \tag{8}$$

This equation differs from the enstrophy equation derived by [23] only from the last term with the third central moment. The quantity $\langle\varepsilon\rangle$ is the depth-averaged dissipation of turbulent kinetic energy. A simple gradient-diffusion model is

$$\left\langle u'^3 \right\rangle = -2\frac{\nu_T}{\sigma}h^2\frac{\partial\varphi}{\partial x} \tag{9}$$

where σ is a turbulent Prandtl number which is generally taken equal to 1 in the models of turbulent flows (see for example [43] p.371). The enstrophy equation becomes

$$\frac{\partial h\varphi}{\partial t} + \frac{\partial hU\varphi}{\partial x} = \frac{8\nu_T}{h}\left(\frac{\partial U}{\partial x}\right)^2 - \frac{2}{h}\langle\varepsilon\rangle + \frac{2}{h^2}\frac{\partial}{\partial x}\left(\frac{\nu_T}{\sigma}h^3\frac{\partial\varphi}{\partial x}\right). \tag{10}$$

An even simpler way to model the last term is to write it in a conservative form as

$$\frac{\partial h\varphi}{\partial t} + \frac{\partial hU\varphi}{\partial x} = \frac{8\nu_T}{h}\left(\frac{\partial U}{\partial x}\right)^2 - \frac{2}{h}\langle\varepsilon\rangle + \frac{\partial}{\partial x}\left(2\frac{\nu_T}{\sigma}h\frac{\partial\varphi}{\partial x}\right). \tag{11}$$

Since the numerical resolution will show that the effect of this term is negligible for reasonable values of σ (i.e. larger than 0.1) except that it helps to smooth the solutions at the breaking point where there is a sudden increase of enstrophy, the main term to be kept is the diffusion term. In practice no difference between (10) and (11) has been noticed in the numerical simulations.

The closure of the model requires expressions for the turbulent viscosity and for the dissipation. As in [23], these expressions are

$$\nu_T = \frac{h^2\sqrt{\varphi}}{R}, \tag{12}$$

where R is a dimensionless quantity which can be interpretated as a Reynolds number, and

$$\langle\varepsilon\rangle = \frac{C_r}{2}h^2\varphi^{3/2}, \tag{13}$$

where C_r is a dimensionless enstrophy dissipation coefficient. This expression of the dissipation guarantees the positivity of the enstrophy. The equations of the model write

$$\frac{\partial h}{\partial t} + \frac{\partial hU}{\partial x} = 0, \tag{14}$$

$$\frac{\partial hU}{\partial t} + \frac{\partial}{\partial x}\left(hU^2 + \frac{gh^2}{2} + h^3\varphi + \frac{h^2\ddot{h}}{3} + \Pi'\right) = \frac{\partial}{\partial x}\left(\frac{4}{R}h^3\sqrt{\varphi}\frac{\partial U}{\partial x}\right) - gh\frac{\partial b}{\partial x} - f', \tag{15}$$

and

$$\frac{\partial h\varphi}{\partial t}+\frac{\partial hU\varphi}{\partial x}=\frac{8h\sqrt{\varphi}}{R}\left(\frac{\partial U}{\partial x}\right)^2-C_r h\varphi^{3/2}+\frac{\partial}{\partial x}\left(2\frac{h^3\sqrt{\varphi}}{\sigma R}\frac{\partial\varphi}{\partial x}\right). \tag{16}$$

The notations $\ddot{h}$, Π' and f' refer to

$$\ddot{h}=h\left(\frac{\partial U}{\partial x}\right)^2-h\frac{\partial^2 U}{\partial x\partial t}-hU\frac{\partial^2 U}{\partial x^2}, \tag{17}$$

$$\Pi'=\frac{h^2}{2}\frac{\mathrm{D}}{\mathrm{D}t}\left(U\frac{\partial b}{\partial x}\right) \tag{18}$$

and

$$f'=h\frac{\partial b}{\partial x}\left[\frac{\ddot{h}}{2}+\frac{\mathrm{D}}{\mathrm{D}t}\left(U\frac{\partial b}{\partial x}\right)\right] \tag{19}$$

where the material derivative is $\mathrm{D}/\mathrm{D}t=\partial/\partial t+U\partial/\partial x$.

These equations are rewritten in an asymptotically equivalent way, firstly to simplify the numerical resolution (§2.2) and secondly to improve the linear dispersive properties (§2.3).

2.2 Asymptotically equivalent model

The model formed by the equations (14), (15) and (16) presents the difficulty for the numerical resolution to have mixed third-order derivatives in space and time in the momentum equation (15). Following the ideas of [4] and [31], an asymptotically equivalent model is derived with a mathematical structure more suited to the numerical resolution. Only the main steps of the method are recalled here and we refer to [31] for the details and justifications.

The equations are written in dimensionless form with a classical scaling (see for example [1]). In particular, the elevation b of the bottom topography is supposed to be of $O(h_0^*)$ and the characteristic length of its variation in the Ox-direction is L. This implies that $\partial b/\partial x=O(\mu)$. In dimensionless form, the momentum equation (15) can be written [23]

$$\frac{\partial hU}{\partial t}+\frac{\partial}{\partial x}\left(hU^2+\frac{h^2}{2}+\mu^{2\beta}h^3\varphi+\mu^2\frac{h^2\ddot{h}}{3}+\mu^2\Pi'\right)$$
$$=\mu^2\frac{\partial}{\partial x}\left(\frac{4}{R}h^3\sqrt{\varphi}\frac{\partial U}{\partial x}\right)-h\frac{\partial b}{\partial x}-\mu^2 f'. \tag{20}$$

In this equation and thereafter, to lighten the notations, the same symbols are used for the dimensionless quantities.

The second derivative (17) is rewritten

$$\frac{h^2\ddot{h}}{3} = -\frac{h^3}{3}\frac{\partial}{\partial x}\left[\frac{1}{h}\left(\frac{\partial hU}{\partial t} + \frac{\partial hU^2}{\partial x}\right)\right] + \frac{2}{3}h^3\left(\frac{\partial U}{\partial x}\right)^2. \tag{21}$$

The terms involving the bottom topography b are reorganized to separate the terms including the material derivative $\mathrm{D}U/\mathrm{D}t$, which necessitates a special treatment, and the other terms. The momentum equation (15) can then be rewritten

$$\begin{aligned}\left(\mathrm{I}+\mu^2\mathrm{T}\right)\left(\frac{\partial hU}{\partial t}+\frac{\partial hU^2}{\partial x}\right) + h\frac{\partial h+b}{\partial x} + \mu^{2\beta}\frac{\partial h^3\varphi}{\partial x} + \mu^2 hQ_1' \\ + \frac{\mu^2}{2}\frac{\partial}{\partial x}\left(h^2\frac{\partial b}{\partial x}\frac{\mathrm{D}U}{\mathrm{D}t}\right) - \mu^2\frac{h^2}{2}\frac{\partial b}{\partial x}\frac{\partial}{\partial x}\frac{\mathrm{D}U}{\mathrm{D}t} + \mu^2 h\left(\frac{\partial b}{\partial x}\right)^2\frac{\mathrm{D}U}{\mathrm{D}t} \\ = \mu^2\frac{\partial}{\partial x}\left(\frac{4}{R}h^3\sqrt{\varphi}\frac{\partial U}{\partial x}\right) + O(\mu^{2+\beta})\end{aligned} \tag{22}$$

where I is the operator identity, T is the operator defined for any quantity W by

$$\mathrm{T}W = -\frac{1}{3}\frac{\partial}{\partial x}\left(h^3\frac{\partial}{\partial x}\frac{W}{h}\right) \tag{23}$$

and

$$\begin{aligned}hQ_1' = \frac{\partial}{\partial x}\left[\frac{2}{3}h^3\left(\frac{\partial U}{\partial x}\right)^2\right] + \frac{\partial}{\partial x}\left(\frac{h^2}{2}U^2\frac{\partial^2 b}{\partial x^2}\right) \\ + h^2\frac{\partial b}{\partial x}\left(\frac{\partial U}{\partial x}\right)^2 + hU^2\frac{\partial b}{\partial x}\frac{\partial^2 b}{\partial x^2}.\end{aligned} \tag{24}$$

The operator T corresponds to the first term at the right-hand side of (21) whereas the quantity Q_1' gathers the terms corresponding to the last term of (21) and all topographic terms which do not include the material derivative $\mathrm{D}U/\mathrm{D}t$. From (22) it is possible to write this material derivative

$$\frac{\mathrm{D}U}{\mathrm{D}t} = -\frac{\partial h+b}{\partial x} + O(\mu^{2\beta}). \tag{25}$$

It is then possible to rewrite consistently (22) with the same precision

$$\begin{aligned}\left(\mathrm{I}+\mu^2\mathrm{T}\right)\left(\frac{\partial hU}{\partial t}+\frac{\partial hU^2}{\partial x}\right) + h\frac{\partial h+b}{\partial x} + \mu^{2\beta}\frac{\partial h^3\varphi}{\partial x} \\ + \mu^2 h\left(Q_1'+Q_2\right) = \mu^2\frac{\partial}{\partial x}\left(\frac{4}{R}h^3\sqrt{\varphi}\frac{\partial U}{\partial x}\right) + O(\mu^{2+\beta})\end{aligned} \tag{26}$$

where

$$hQ_2 = \frac{h^2}{2}\frac{\partial b}{\partial x}\frac{\partial^2 h+b}{\partial x^2} - \frac{1}{2}\frac{\partial}{\partial x}\left(h^2\frac{\partial b}{\partial x}\frac{\partial h+b}{\partial x}\right) - h\left(\frac{\partial b}{\partial x}\right)^2\frac{\partial h+b}{\partial x}. \quad (27)$$

The method of using this asymptotically equivalent formulation was first proposed by [4]. The advantage of this method is that the system can be solved without any third-order derivative. However this operator is time-dependent which makes its inversion time-consuming. The final step is the constant method which introduces a time-independent operator by using the following asymptotically equivalent equation [31]

$$\left(\mathrm{I}+\mu^2\mathbb{T}\right)\left(\frac{\partial hU}{\partial t}+\frac{\partial hU^2}{\partial x}\right) + h\frac{\partial h+b}{\partial x} + \mu^{2\beta}\frac{\partial h^3\varphi}{\partial x} + \mu^2 h\left(Q_1' + Q_2\right) + Q_3 = \mu^2\frac{\partial}{\partial x}\left(\frac{4}{R}h^3\sqrt{\varphi}\frac{\partial U}{\partial x}\right) + O(\mu^{2+\beta}) \quad (28)$$

where the time-independent operator $\mathbb{T}$ is defined for any quantity W by

$$\mathbb{T}W = -\frac{1}{3}\frac{\partial}{\partial x}\left(h_0^3\frac{\partial}{\partial x}\frac{W}{h_0}\right) \quad (29)$$

and

$$Q_3 = \mathrm{S}\left[\left(\mathrm{I}+\mu^2\mathbb{T}\right)^{-1}\left(h\frac{\partial h+b}{\partial x}\right)\right] \quad (30)$$

where the operator S is defined for any quantity W by

$$\mathrm{S}W = \frac{1}{6}\frac{\partial h^2-h_0^2}{\partial x}\frac{\partial W}{\partial x} + \frac{1}{3}\left(h^2-h_0^2\right)\frac{\partial^2 W}{\partial x^2} - \frac{1}{6}\frac{\partial^2 h^2-h_0^2}{\partial x^2}W. \quad (31)$$

The operator $\mathrm{I}+\mu^2\mathbb{T}$ is inverted only once at the beginning of the numerical resolution, using the still water depth. This method decreases markedly the computation time and is efficient and robust [31].

2.3 Optimization of the dispersive properties

The Serre-Green-Naghdi equations are weakly dispersive. Their dispersive properties are accurate while the depth is not too large, more precisely until $kh_0 \simeq 1$ [11] where k is the wavenumber. For practical applications, a larger validity domain is often required which implies to use an optimization technique. The optimization procedure of [4] can be easily adapted to this

system. An asymptotically equivalent system is derived, once again using (25). It is then possible to write

$$\mu^2\mathbb{T}\left(\frac{\partial hU}{\partial t}+\frac{\partial hU^2}{\partial x}\right)=\mu^2\alpha\mathbb{T}\left(\frac{\partial hU}{\partial t}+\frac{\partial hU^2}{\partial x}\right)+\mu^2\left(\alpha-1\right)\mathbb{T}\left(h\frac{\partial h+b}{\partial x}\right)+O(\mu^{2+2\beta}) \quad (32)$$

where $\alpha > 1$. This gives the following asymptotically equivalent system with improved dispersive properties

$$\left(\mathrm{I}+\mu^2\alpha\mathbb{T}\right)\left(\frac{\partial hU}{\partial t}+\frac{\partial hU^2}{\partial x}+\frac{\alpha-1}{\alpha}h\frac{\partial h+b}{\partial x}\right)+\frac{1}{\alpha}h\frac{\partial h+b}{\partial x}+\mu^{2\beta}\frac{\partial h^3\varphi}{\partial x}+\mu^2h\left(Q_1'+Q_2\right)+Q_3=\mu^2\frac{\partial}{\partial x}\left(\frac{4}{R}h^3\sqrt{\varphi}\frac{\partial U}{\partial x}\right)+O(\mu^{2+\beta}), \quad (33)$$

together with the mass equation (14) and the enstrophy equation (16). The optimal value of α is [4]

$$\alpha = 1.159. \quad (34)$$

With this value the phase velocity is accurate until $kh_0 \simeq 4.5$, the group velocity until $kh_0 \simeq 2.5$ and the shoaling coefficient until $kh_0 \simeq 2$ [4], [11].

3 Numerical aspects

Neglecting the $O(\mu^{2+\beta})$ residuals in (33) and going back to variables with dimensions, the final set of equations, completed with (14) and (16), is discretized on the basis of the Discontinuous Galerkin scheme proposed by [16], originally designed for the 1D Serre-Green-Naghdi equations. From a numerical viewpoint, the extension to the present model consists in a slight modification of the momentum equation and the addition of a transport equation in the discrete formulation. This can be done without particular technical difficulties, and the reader is referred to [16] for implementation details (see [46] for the 2D case).

As regards the wave-breaking treatment, we follow the strategy proposed by [23]. As reported in this work, injecting enstrophy at the very beginning of the computations may have an impact on the amplitude of the waves, even outside breaking areas. To prevent this, the idea is to turn on viscous (creation) terms in the enstrophy equation only when needed. To achieve

this, a breaking criterion is used, relying on the concept of *virtual enstrophy*, denoted ψ in the sequel. This new quantity satisfies a second transport equation, introduced to evaluate the amount of enstrophy that the model is able to produce, but without retroaction on the physical flow variables. Put in other words, the virtual enstrophy is computed exactly as the enstrophy, with viscous terms evaluated in the whole computational domain. Wave breaking can then be characterized by a sudden growth of virtual enstrophy. In practice, breaking areas are identified as those for which $\psi > \psi_0$, (with ψ_0 a threshold to be defined) resulting in a local activation of the viscous terms in the *effective* enstrophy equation. It should be noted, however, that the use of such a tool is unnecessary for simulations implying small relative amplitudes. Following [23], the trigger threshold is thus defined as:

$$\psi_0 = \psi_{0s} = \begin{cases} \dfrac{g}{h_0}\left(0.1 + 0.031\dfrac{h_0^*}{a}\right) \text{ if } \dfrac{a}{h_0^*} > 0.05\,, \\ 0 \text{ otherwise}\,. \end{cases} \tag{35}$$

with h_0^* the still water depth at the initial position of the wave and a the initial amplitude of the wave. Regarding the other parameters of the model, the (dimensionless) Reynolds number is given by

$$R = R_0 = 0.85 + 60\,s\,, \tag{36}$$

s being the bed slope, and the dissipation coefficient present in (16) has the universal value $C_r = 0.48$. The eddy viscosity can be written

$$\nu_T = B\frac{h^2\sqrt{\varphi}}{R} \tag{37}$$

with $B = 0$ where $\psi < \psi_0$ and $B = 1$ elsewhere. Note that these choices proved to be relevant in a large variety of 1D and 2D applications implying solitary waves propagating over non-trivial topographies (see [23, 46]), thus conferring a predictive character to the model. The main purpose of the present work is to investigate its applicability to wave trains. As will be seen through the next examples, although being almost immediate, some specific aspects must be taken into account. The main reason is that the enstrophy produced by a single wave is not always dissipated during one period, and may be partially recovered by the following ones. This can lead to an accumulation phenomenon at the level of the breaking point, resulting in a slight underestimation of the wave's amplitude. Note that these observations are in accordance with the complex turbulent interactions induced by wave trains reported in experimental works (see for instance [54]). We shall see that a small increase of the Reynolds number or the breaking threshold is sufficient to remedy this problem.

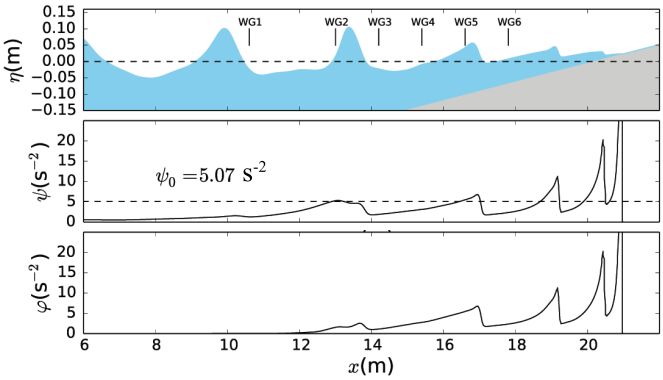

Figure 2: Cox's experiment - Snapshot of the flow during the propagation, together with gauges location (*top*). Corresponding spatial distribution of the virtual (*middle*) and effective enstrophy (*bottom*).

4 Model validation

4.1 Cox's experiment [13]

The first test we consider is based on the experimental study carried out by [13] and implies a regular train of cnoidal waves with relative amplitude $a/h_0^* = 0.29$, and period $T = 2.2\,\mathrm{s}$, propagating in a wave flume with a constant bed slope 1/35. The still water level h_0^* in the constant depth section of the channel is $h_0^* = 0.4\,\mathrm{m}$. In this context, as the waves approach the shore, they start shoaling under the effect of the topogaphy, steepen and experience breaking of spilling type. The objective is therefore to evaluate the capacity of the present model to faithfully reproduce these characteristics. The computational domain is $[0, 24]$ and includes a sponge layer of 5 m at the left boundary to allow a proper generation of incident waves. The topography is parametrized as follows:

$$z(x) = \max\left(0, \frac{x-6}{35}\right). \tag{38}$$

The time evolution of the free surface was recorded at six wave gauges, located at $x = 10.6\,\mathrm{m}$, $x = 13\,\mathrm{m}$, $x = 14.2\,\mathrm{m}$, $x = 15.4\,\mathrm{m}$, $x = 16.6\,\mathrm{m}$ and $x = 17.8\,\mathrm{m}$ as indicated in Fig. 2 (*top*). Note that the present configuration leads to $\psi_0 = \psi_{0s} = 5.07\,\mathrm{s}^{-2}$ for the breaking threshold. As can be seen on Fig. 2 (*middle*), this limit value is reached around $x = 13\,\mathrm{m}$, between WG2 and WG3, which marks the beginning of the breaking area. This is in accordance with the experiments and other numerical results [57]. From this point we clearly see local entropy peaks follow the breaking of the waves

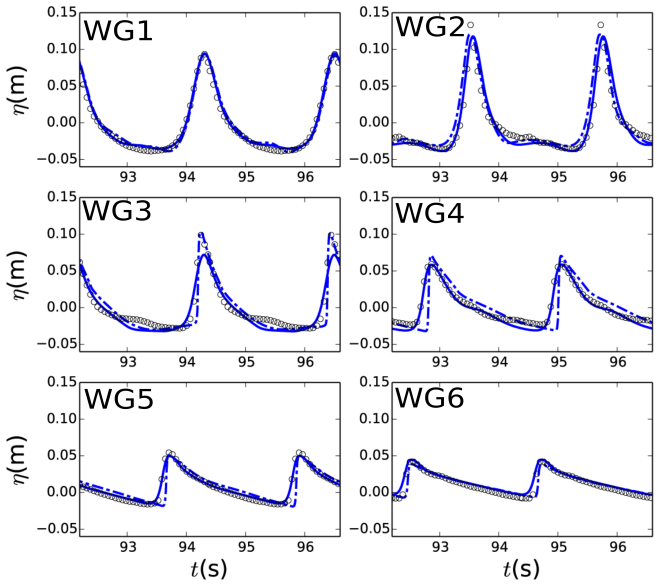

Figure 3: Cox's experiment - Comparison between experimental (*circles*) and numerical time-series of the free surface elevation, obtained with a switching strategy (-.-) and the present model (solid curve).

until the shore. As noted above, looking at virtual and effective enstrophy (Fig. 2 *middle* and *bottom*), we also observe that the turbulent energy of the model $h^2\varphi/2$ has no time to completely dissipate between two successive waves, which is in accordance with the results found by [54] and [56] on spilling-type breaking. Part of this energy is thus reintroduced in the train, with the effect of slightly decreasing the wave's amplitude. As mentioned, one possibility is to increase the Reynolds number to balance this residual turbulent energy. In the presented results, it is fixed to $R = 1.2R_0 = 3.08$, where R_0 is the Reynolds number given by (36).

Comparison with experimental time series of the free surface are available in Fig. 3, together with numerical results obtained with a classical switching strategy. We observe an overall good agreement, especially for the three last gauges, where the present model seems in better agreement with structural aspects of the wave. In particular, breaking waves treated as shock with the switching method tend to present steeper fronts, notably at gauge WG4 and WG5 where the present model gives a more accurate profile.

For both strategies we also notice an underestimation of the wave height at the breaking point, which is characteristic of the Serre-Green-Naghdi solutions. These observations are supported by Fig. 4, giving the spatial distribution of the amplitudes and mean value of the free surface (*top*), wave

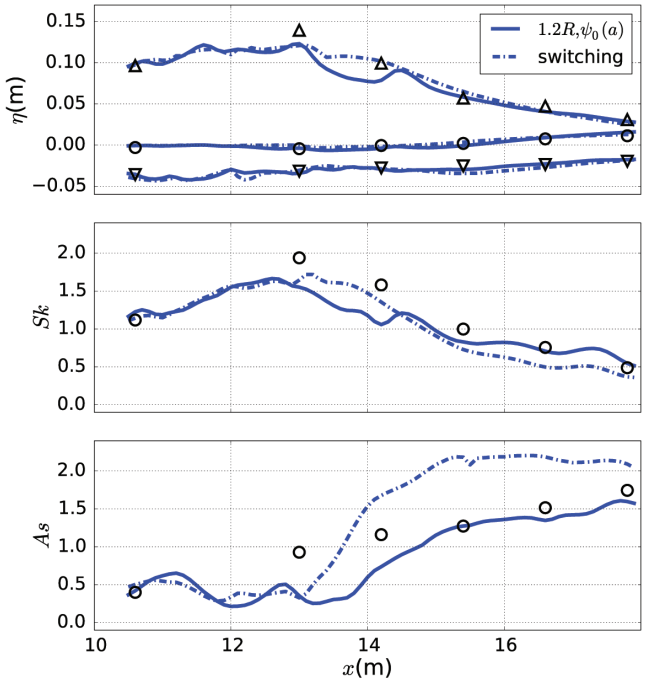

Figure 4: Cox's experiment - Spatial evolution of several diagnostic quantities around the breaking point. Comparison between experimental measurements (*symbols*), numerical results obtained with a switching strategy (-.-), and the present model (*solid curves*) . *Top* : Mean Water Level (o), crest elevation relative to MWL ($\triangle$), trough elevation relative to MWL ($\triangledown$). *Middle:* Wave skewness. *Bottom:* Wave asymmetry.

skewness Sk (*middle*) and wave asymmetry As (*bottom*). These two last quantities are computed as follows [26]:

$$Sk = \frac{\overline{(\eta - \bar{\eta})^3}}{\overline{(\eta - \bar{\eta})^2}^{3/2}}\,, \tag{39}$$

$$As = \frac{\overline{\mathcal{H}(\eta - \bar{\eta})^3}}{\overline{(\eta - \bar{\eta})^2}^{3/2}}\,, \tag{40}$$

where $\mathcal{H}$ stands for the Hilbert transform, $\bar{\eta}$ is the mean elevation and $\overline{X}$ is the time-averaged value of any quantity X. Both models are in agreement with the experiments in the shoaling zone (before 12 m). There are some discrepancies in the breaking zone (around 13–14 m) since no depth-averaged model can describe accurately the breaking process and because the Serre-Green-Naghdi equations tend to predict waves less peaked than observed waves and thus with a lower skewness. In the inner surf zone (after 15 m), the present model improves significantly the skewness factor and the asymmetry factor compared to the switching model. The switching approach underestimates the skewness in the inner surf zone and overestimates markedly the asymmetry. Since the switching model treats the front of breaking waves as a shock, the predicted asymmetry should be much higher than the experimental values. The numerical viscosity can decrease somewhat this discrepancy resulting in a deterioration of the solution with mesh refinement in the case of the switching model.

The calculated mean water level (MWL) is in agreement with the experiments including the small set-down effect and the set-up effect. The crest and trough elevations relative to the mean water level are also correctly reproduced except, as noted above, the crest elevation at the breaking point (gauges WG2 and WG3).

Numerical convergence was reached with a space step of $\Delta x = 0.02$ m. A fundamental advantage of the present approch over switching-type strategies relies on its low sensitivity with respect to the space discretization parameters. Indeed, very similar results were obtained at higher orders and for more important mesh resolutions. Reversely, switching strategies are less robust since a modification of the space step may entail significant variations of the numerical results, and require a new calibration of the breaking parameters (see [57, 25]). Furthermore, in the case of the switching model, spurious oscillations appear with mesh refinement and these numerical instabilities increase if the cells become thinner which prevents mesh convergence. This problem does not take place with our model.

4.2 Ting and Kirby's experiment [54]

Based on the same experimental set-up, [54, 55] conducted a series of works dedicated to the study of breaking wave trains of spilling and plunging type. We first focus on the spilling breaker case, corresponding to a wave period $T = 2\,\mathrm{s}$ and an amplitude $a = 0.125\,\mathrm{m}$. Computations are run on the interval $[0, 40]$ and we consider the following topography:

$$z(x) = \max\left(0, \frac{x - 10}{35}\right). \tag{41}$$

Based on the empirical laws (35), (36), the optimal choice for the breaking constants is $R = 1.3R_0 = 3.3$ and $\psi_0 = 1.3\,\psi_{0s} = 6.3\,\mathrm{s}^{-2}$, where ψ_{0s} is the value given by (35), which are almost the same values as for Cox's experiments. The numerical results were obtained for a mesh size $\Delta x = 0.04\,\mathrm{m}$.

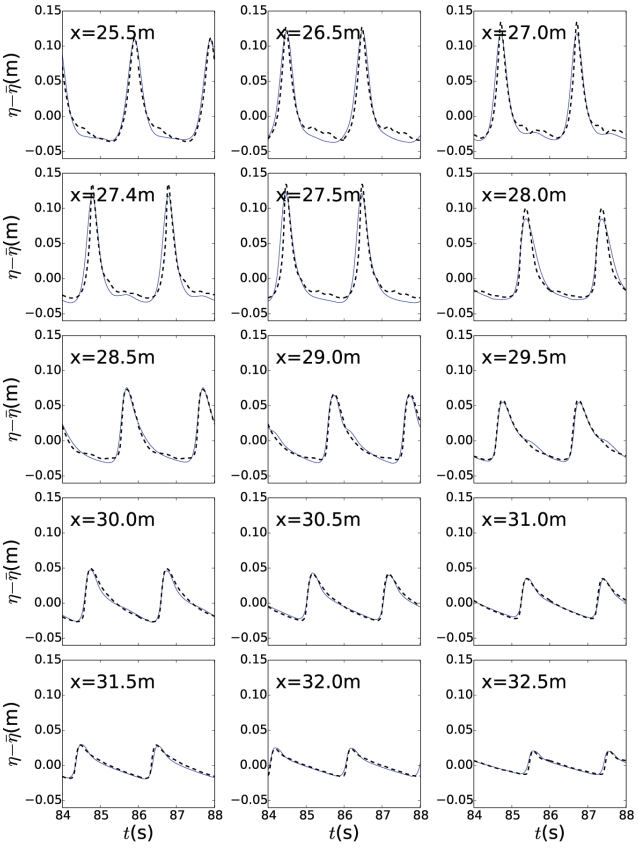

Figure 5: Ting and Kirby's experiment - Spilling breaker : Comparison between experimental and numerical time-series of the free surface elevation.

Comparisons between measured and simulated time-series of the free surface elevation at several wave gauges located along the domain are available on Fig. 5. We can observe an overall good agreement, except at the breaking point (around 27–28 m) where the waves have a smaller amplitude and are wider and less peaked. We also note that the wave characteristics are particularly well reproduced in the inner surf zone (after 28 m). In particular, we recover the expected amplitudes and observe a faithful reproduction of the steepness profiles.

These observations are confirmed by the skewness and asymmetry calculations available in Fig. 6 (*middle* and *bottom*, respectively). In particular, the estimation of the asymmetry indicators marks a noticeable improvement when compared to switching-type strategies [57]. Surface elevation profiles, including wave crest, wave trough and mean elevation are given in Fig. 6 (*top*), exhibiting a good agreement with the experiment, in line with other works available in the literature (see [12, 36, 57]). The skewness coefficient is too small in the breaking zone, because the waves are wider and lower, but is correctly estimated in the inner surf zone. The mean water level presents a noticeable set-down effect at 28 m which was not measured in the experiments and a set-up effect in accordance with the measured values. The crest and trough elevations relative to the mean water level are in agreement with the experiments except for a lower crest elevation at the breaking point.

The ability of the model to describe the evolution of the turbulent energy can be assessed through Fig. 7. The time-series of the dimensionless turbulent energy are presented, as well as the dimensionless velocity, at three wave gauges located in the inner surf zone. As in the previous case, the amount of enstrophy produced by the mechanism of breaking is not dissipated during one period. A large proportion is still present in time windows associated with a negative velocity, which means that a substantial part of the turbulent energy is carried offshore. This result is qualitatively in accordance with [54] who found that the turbulent kinetic energy is transported seaward under the spilling breaker.

Keeping the same discretization parameters, we now turn to the case of the plunging breaker studied by [55]. The period is $T = 5\,\mathrm{s}$ and the amplitude is $a = 0.128\,\mathrm{m}$. The optimal parameters of the model are $R = 1.2\,R_0 = 3.1$ and $\psi_0 = 1.1\,\psi_{0s} = 5.3\,\mathrm{s}^{-2}$.

The distributions of wave amplitudes and mean water level given in Fig. 8 are well reproduced when comparing to experimental results of [54]. As for the spilling breaker case, a small set-down effect is noticeable in the mean water level curve which was not measured in the experiments. The set-up at the end of the inner surf zone is in agreement with the measures. The calculated crest and trough elevations are very closed to the experimental

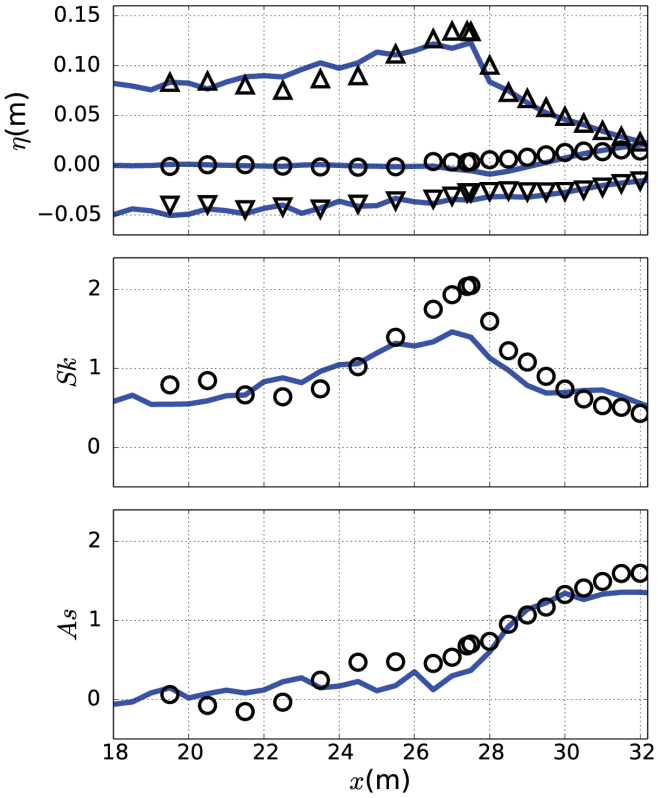

Figure 6: Ting and Kirby's experiment - Spilling breaker : Spatial evolution of several diagnostic quantities around the breaking point. Comparison between experimental measurements (*symbols*), numerical results obtained with the present model (*solid curves*). *Top* : Mean Water Level (o), crest elevation relative to MWL ($\triangle$), trough elevation relative to MWL ($\triangledown$). *Middle:* Wave skewness. *Bottom:* Wave asymmetry.

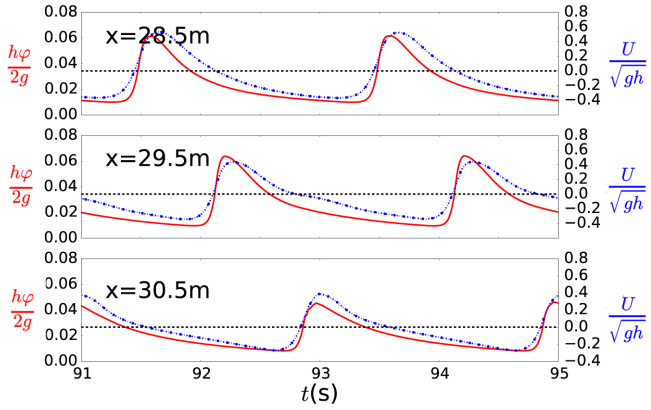

Figure 7: Ting and Kirby's experiment - Spilling breaker : time-series of the dimensionless velocity $U/\sqrt{gh}$ (*dotted curves*) and the dimensionless turbulent energy $h\varphi/2g$ (*solid curves*) at the level of the breaking point. Zero velocity reference appears in dashed lines.

results, even the maximum value of the crest elevation at the breaking point which is similar to the experimental value.

The results available in Fig. 9 highlight a notable difference with spilling breakers. At the level of the breaking point, we note that the turbulent energy produced by a single wave has time to dissipate almost completely before the following wave, so that each wave is handled independently by its own enstrophy production. As a result, the amount of turbulent energy carried offshore is very low, marking a sharp distinction with respect to spilling breakers. The turbulent energy of the model is very small when the averaged velocity is negative (seaward) which means that the overall turbulent energy transport is shoreward. This is in agreement with the result of [54] who noted that in the case of the plunging breaker the turbulent kinetic energy is transported landward and that it is dissipated within one wave cycle.

The model is thus able to predict the variations of the turbulent energy and the direction of its transport and to distinguish between the case of a short wave period, such as the spilling breaker with $T = 2\,\mathrm{s}$ of [56], where the turbulent energy is not dissipated within one wave cycle resulting in a seaward transport, and the case of a longer wave period, as the case of the plunging breaker with $T = 5\,\mathrm{s}$ of [55], where the turbulent energy is dissipated in one period and transported landward.

Note that the measurements of the turbulent kinetic energy of [55] and [56] cannot be quantitatively compared to our numerical results because the turbulent energy of the model is a depth-averaged quantity and includes not only the large-scale turbulence but also the depth variation of the mean

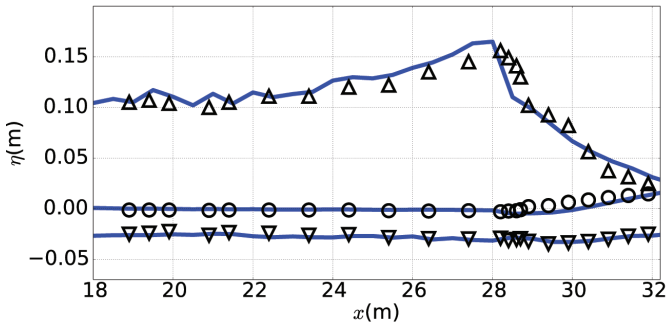

Figure 8: Ting and Kirby's experiment - Plunging breaker : Comparison between experimental measurements (*symbols*) and numerical results obtained with the present model (*solid curves*). *Top* : Mean Water Level (o), crest elevation relative to MWL ($\triangle$), trough elevation relative to MWL ($\triangledown$). *Middle:* Wave skewness. *Bottom:* Wave asymmetry.

velocity (which means that this "turbulent" energy includes a non-turbulent component) whereas the turbulent kinetic energy is measured by [56] at a specific depth and does not include the variation of the mean velocity. In particular there is no experimental measures in the highest part of the flow, near the free surface, where the turbulent kinetic energy has often its highest values (see for example the measures of [27]). Furthermore the variation with the depth of the mean velocity gives a contribution of the same order of magnitude as the turbulent kinetic energy itself to the depth-averaged "turbulent" energy of the model. This explains that our values are higher but qualitatively similar.

4.3 Study of wave set-down

The purpose of this section is to study, in the case of the experiments of [6], the characteristic variations of the mean water level induced by the presence of wave trains and in particular the set-down phenomenon, corresponding to the characteristic depression of the mean water level observed near the breaking point. The calculated set-down is governed by the dispersive properties of the model. The experiment includes propagation, breaking and run-up of a train of regular sinusoidal waves. Several configurations studied by [6] have been studied with different wavelengths and initial amplitudes. For instance the experiment with a wavelength of $\lambda = 2.02\,\mathrm{m}$, a period of $T = 1.14\,\mathrm{s}$ and a deep water wave height of $H_0 = 6.45\,\mathrm{cm}$ leads to a computed value of $-0.37\,\mathrm{cm}$ compared to the still water level whereas the experimental set-down was measured by [6] at $-0.32\,\mathrm{cm}$. Similar results were obtained for the

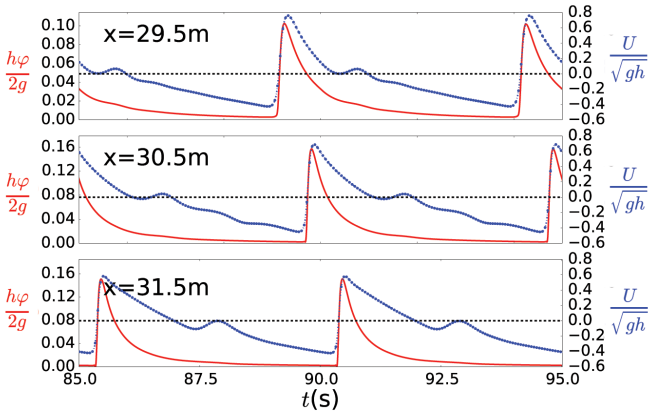

Figure 9: Ting and Kirby's experiment - Plunging breaker : time-series of the dimensionless velocity $U/\sqrt{gh}$ (*dotted*) and the dimensionless turbulent energy $h\varphi/2g$ (*lines*) at the level of the breaking point.

other configurations. Overall, the model overestimates the set-down effect (the calculated mean water level is lower than the measured one) by 10–20% approximately. This is consistent with what is commonly noticed in other models.

4.4 Breaking of irregular waves [3]

On the basis of the experimental study of [3], we now investigate the behaviour of the proposed breaking model in the context of irregular waves. Beji and Battjes conducted a series of experiments implying regular and irregular wave trains propagating over a submerged bar. The experimental basin is 37.7 m long, 0.8 m wide and is equipped with a trapezoïdal bar extending from $x = 10$ m to $x = 15$ m, with 1/20 front and 1/10 back slopes. We initially consider a flow at rest with a total depth $h_0^* = 0.4$ m. Among the experimental data set available, we focus on JONSWAP type random waves breaking above the bar as spilling breakers, corresponding to a peak period $T = 2.5$ s, and a characteristic frequency $f = 0.4$ Hz. The time evolution of the free surface was recorded at eight experimental gauges, represented in Fig. 10 (*top*). The signal available at the first wave gauge WG1 ($x = 6$ m) is used to impose the initial condition at the left boundary.

Note that as in the case of the experiments of [3] on regular waves [46], due to the relatively small nonlinearity of the incident waves involved in this test, no breaking criterion is needed here (in other terms, we use $\psi_0 = 0$). According to [23] and [46] the admissible range for the dimensionless Reynolds number is $5 \leq R \leq 10$ for waves with a small nonlinearity such that no break-

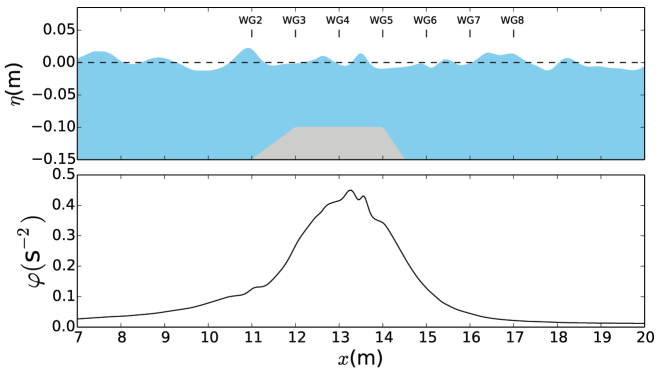

Figure 10: Breaking of irregular waves - Snapshot of the flow during the propagation, together with gauges location (*top*). Corresponding spatial distribution of the enstrophy (*bottom*).

ing criterion is used. The value $R = 5$ is chosen. Also, numerical results with $R = 9.5$ are also proposed for the sake of completeness. Comparison between measured and simulated time-series of the free surface elevation are proposed at WG2 ($x = 11\,\mathrm{m}$), WG5 ($x = 14\,\mathrm{m}$) and WG7 ($x = 16\,\mathrm{m}$) within the time window [200 s, 230 s].

We observe a very good agreement on all gauges (Fig. 11). In particular, the flow experiences a significant increase of enstrophy at the level of the flat part of the bar, corresponding to the breaking area identified experimentally (Fig. 10). Comparisons with experimental data at WG5 and WG7 given in Fig. 11 also indicate a good behaviour of the numerical solution at the rear side of the bar, able to reproduce correctly the free surface deformations with an accurate estimation of the amplitudes. Contrary to many models, this experiment on irregular waves can be simulated with our model with a good accuracy without any breaking criterion, neither for the breaking initiation nor for the breaking termination.

Repartition of the experimental and numerical spectral density with respect to frequency is proposed in Fig. 12, in which we clearly recognize the first harmonic at $f = 0.4\,\mathrm{Hz}$. The present model is also able to capture the second peak frequency at $f = 0.8\,\mathrm{Hz}$, even at the last gauges. The highest harmonics are damped due to a residual viscosity which is still present after breaking. The damping effect is significantly reduced if R is increased from $R = 5$ to $R = 9.5$ because this decreases the viscosity. Indeed, as evidenced by Fig. 12, setting the viscous terms artificially to zero shortly after breaking reduces almost completely the damping effect on the high frequencies, improving the simulation of the free surface in the rapidly varying parts (Fig. 11). More precisely, in the case $R = 9.5$ and $\nu_{x>14\,\mathrm{m}} = 0$, we locally set

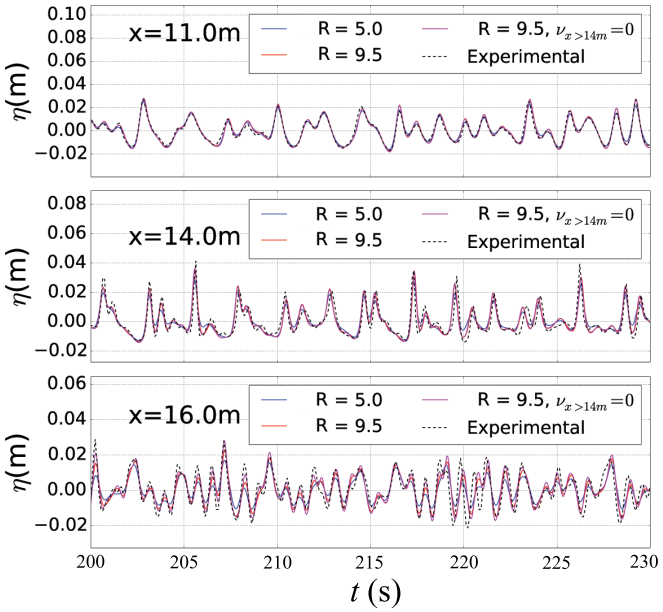

Figure 11: Breaking of irregular waves - Time evolution of the free surface and enstrophy flux at WG2, WG5 and WG7 for two different Reynolds numbers. Comparison with experimental data.

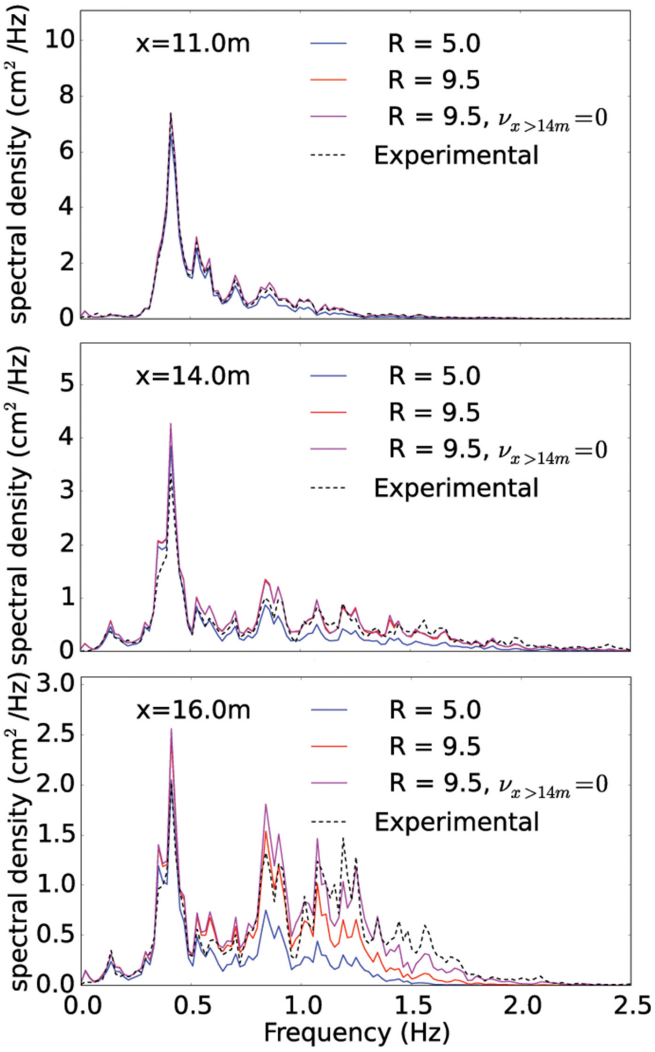

Figure 12: Breaking of irregular waves (colour online) - Spectral density of the signal at gauges 2, 5 and 7. Comparison with the spectrum of the experimental results.

$\nu_T = 0$ from $x = 14\,\mathrm{m}$ in (16) and (33). Even if the free surface elevation is correctly reproduced in all simulations with small differences, the nonlinear phenomenon of high-frequency generation in the shallow horizontal part above the bar and in the deepening part of the propagation is better simulated with $R = 9.5$ which gives a satisfactory treatment of the nonlinear interactions.

5 Conclusion

In this work the recent model of [23] and [46] for coastal waves, mainly dedicated to solitary waves, was supplemented with a turbulent diffusion term and extended to the case of regular and irregular wave trains. The model is fully nonlinear and has the same dispersive properties as the Green-Naghdi equations, but is also able to account for the large-scale turbulence and the depth variations of the mean velocity through a new variable called enstrophy. The new diffusive term is useful only for the numerical treatment to smooth the solutions at the breaking point.

The turbulent dissipation coefficient C_r has a universal value (0.48) and needs no calibration. In the case of waves with a small nonlinearity, as in the experiments of [3], no breaking criterion is needed and we found that the values in the range given in [23] for the turbulent Reynolds number can be used, preferably at the upper bound to minimize the attenuation of the high-frequency harmonics generated near the coast. For wave trains with a higher nonlinearity, the breaking criterion of [23] can be used with the same empirical laws for the turbulent Reynolds number and for the breaking threshold except that the values of these two dimensionless quantities should be increased by up to 30% in the case of the wave trains studied in this paper.

The model includes a term in the energy equation which is called turbulent energy but which includes, in a depth-averaged sense, the large-scale turbulence and the non-uniformity in the depth of the mean velocity. The variations of this turbulent energy in a wave train are qualitatively in agreement with the experimental measures of [54] on the transport of the turbulent kinetic energy: in the case of the spilling breakers with a short wavelength [56], the turbulent energy is not dissipated within one wave cycle and it is mostly transported seaward since it keeps an important value when the depth-averaged velocity is seaward (this can be interpretated as the effect of the undertow); in the case of the plunging breakers [55], because of the longer wave period, the turbulent energy is dissipated within one wave cycle and keeps significative values only in the part of the wave where the averaged velocity is shoreward, giving a shoreward transport of the turbulent energy.

The simulation of irregular waves over a bar shows that the nonlinear effects due to shoaling, breaking, propagation in a shallow horizontal part and de-shoaling are correctly reproduced, including the generation of higher harmonics. The model predicts accurately the set-up phenomenon but overestimates slightly the set-down effect and underestimates the wave amplitude at the breaking point. The calculated skewness and asymmetry coefficients are underestimated in the breaking zone but they are in agreement with the experiments in the inner surf zone. The deviations in the breaking zone are

common to many models including the Serre-Green-Naghdi models but, compared to the switching approach, the present model improves significantly the asymmetry coefficient of the breaking waves in the inner surf zone.

From a numerical point of view the model is more robust than the switching approach because of its low sensitivity to the space discretization parameters and its ability to reach the numerical convergence. The predictive ability of the model is interesting since the empirical laws give the values of the one or two variable dimensionless parameters with very little tuning but of course it should be tested in an even wider range of situations before reaching definitive conclusions on this matter. This model would be significantly improved if the need for a breaking criterion could be removed in all cases whereas such a criterion is presently needless only in the case of waves with a small nonlinearity.

Acknowledgments

The work has been partially supported by the French National Research Agency project NABUCO, grant ANR-17-CE40-0025, the Service Hydrographique et Océanographique de la Marine (SHOM), project MEPELS, and the french INSU-CNRS (Institut National des Sciences de l'Univers - Centre National de la Recherche Scientifique) program LEFE-MANU (Méthodes Mathématiques et Numériques), project DWAVE.

References

[1] Antuono, M. and Brocchini, M. Beyond Boussinesq-type equations: semi-integrated models for coastal dynamics. *Phys. Fluids* **25**, 016603, 2013.

[2] Barthélemy, E. Nonlinear shallow water theories for coastal waves. *Surveys in Geophysics* **25**, 315–337, 2004.

[3] Beji, S. and Battjes, J. A. Experimental investigations of wave propagation over a bar. *Coast. Eng.* **19**, 151–162, 1993.

[4] Bonneton, P., Chazel, F., Lannes, D., Marche, F. & Tissier, M. A splitting approach for the fully nonlinear and weakly dispersive Green-Naghdi model. *J. Comput. Phys.* **230**, 1479–1498, 2011.

[5] Boussinesq, J. Théorie des ondes et des remous qui se propagent le long d'un canal rectangulaire horizontal, en communiquant au liquide contenu dans ce canal des vitesses sensiblement pareilles de la surface au fond. *J. Mathématiques Pures et Appliquées. Deuxième Série* **17**, 55–108, 1872.

[6] Bowen, A.J. and Inman, D.L. and Simmons, V.P. Wave set-down and Set-up. *Journal of Geophysical Research* **73**, 2569–2577, 1968.

[7] Briganti, R. and Musumeci, R.E. and Bellotti, G. and Brocchini, M. and Foti, E. Boussinesq modeling of breaking waves: description of turbulence. *Journal of Geophysical Research* **109**, C07015, 2004.

[8] Brocchini, M. A reasoned overview on Boussinesq-type models: the interplay between physics, mathematics and numerics. *Proc. R. Soc. A* **469**, 2013.

[9] do Carmo, J. S. A., Ferreira, J. A., Pinto, L. & Romanazzi, G. An improved Serre model: Efficient simulation and comparative evaluation. *Appl. Math. Model.* **56**, 404–423, 2018.

[10] Castro, A. and Lannes, D. Fully nonlinear long-wave models in the presence of voticity. *Journal of Fluid Mechanics* **759**, 642–675, 2014.

[11] Chazel, F. and Lannes, D. and Marche, F. Numerical Simulation of Strongly Nonlinear and Dispersive Waves Using a Green–Naghdi Model. *Journal of Scientific Computing* **48**, 105–116, 2011.

[12] Cienfuegos, R., Barthelemy, E., Bonneton, P. Wave-breaking model for Boussinesq-type equations including roller effects in the mass conservation equation. *J. Waterway Port Coast. Ocean Eng.* **136**, 10–26, 2010.

[13] Cox, D.T. Experimental and numerical modelling of surf zone hydrodynamics. *Research report ; no. CACR-95-07 Research report (University of Delaware. Dept. of Civil Engineering. Center for Applied Coastal Research) ; CACR-95-07.*, 1995.

[14] Derakhti, M., Kirby, J. T., Shi, F., & Ma, G. NHWAVE: Consistent boundary conditions and turbulence modeling. *Ocean Model.* **106**, 121–130, 2016.

[15] Derakhti, M., Kirby, J. T., Shi, F., & Ma, G. Wave breaking in the surf zone and deep-water in a non-hydrostatic RANS model. Part 1: Organized wave motions. *Ocean Model.* **107**, 125–138, 2016.

[16] Duran, A. and Marche, F. newblock Discontinuous Galerkin discretization of a new class of Green-Naghdi equations. *Commun. Comput. Phys.* **17**, 721–760, 2015.

[17] Duran, A. and Marche, F. A discontinuous Galerkin method for a new class of Green-Naghdi equations on simplicial unstructured meshes *Appl. Math. Model.* **45**, 840–864, 2017.

[18] Filippini, A. G., Kazolea, M. & Ricchiuto, M. A flexible genuinely nonlinear approach for nonlinear wave propagation, breaking and run-up. *J. Comput. Phys.* **310**, 381–417, 2016.

[19] Gavrilyuk, S. and Liapidevskii, V.Yu. and Chesnokov, A.A. Spilling breakers in shallow water: applications to Favre waves and to the shoaling and breaking of solitary waves. *Journal of Fluid Mechanics* **808**, 441–468, 2016.

[20] Green, A. E. and Laws, N. and Naghdi, P. M. On the theory of water waves. *Proc. R. Soc. London* **338**, 43–55, 1974.

[21] Green, A. E. and Naghdi, P. M. A derivation of equations for wave propagation in water of variable depth. *J. Fluid Mech.* **78**, 237–246, 1976.

[22] Heitner, K.L. and Housner, G.W. Numerical model for Tsunami runup *J. Waterways Ports. Coast. and Ocean Eng.* **96**, 701–719, 1970.

[23] Kazakova, M. & Richard, G. L. A new model of shoaling and breaking waves: One-dimensional solitary wave on a mild sloping beach. *Journal of Fluid Mechanics*, **862**, 552–591, 2019.

[24] Kazolea, M., Delis, A. I. & Synolakis, C. E. Numerical treatment of wave breaking on unstructured finite volume approximations for extended Boussinesq-type equations. *J. Comput. Phys.* **271**, 281–305, 2014.

[25] Kazolea, M. & Ricchiuto, M. On wave breaking for Boussinesq-type models. *Ocean Model.* **123**, 16–39, 2018.

[26] Kennedy, A.B. and Chen, Q. and Kirby, J.T. and Dalrymple, R.A. Boussinesq modeling of wave transformation, breaking and runup *J. Waterway Port Coast. Ocean Eng.* **126**, 39–47, 2000.

[27] Kimmoun, O. & Branger, H. A particle image velocimetry investigation on laboratory surf-zone breaking waves over a sloping beach. *Journal of Fluid Mechanics*, **588**, 353–397, 2007.

[28] Kirby, J. T. Boussinesq models and their application to coastal processes across a wide range of scales. *J. Waterway Port Coast. Ocean Eng.* **142**, 03116005, 2016.

[29] Karambas, T. and Tozer, N. Breaking waves in the surf and swash zone. *Journal of Coastal Research.* **19**, 514–528, 2003.

[30] Lannes, D. & Bonneton, P. Derivation of asymptotic two-dimensional time-dependent equations for surface water wave propagation. *Phys. Fluids.* **21**, 016601, 2009

[31] Lannes, D. & Marche, F. A new class of fully nonlinear and weakly dispersive Green-Naghdi models for efficient 2D simulations. *J. Comput. Phys.* **282**, 238–268, 2015

[32] Lilly, D. K. The representation of small-scale turbulence in numerical simulation experiments. In *Proc. IBM Scientific Computing Symp. on Environmental Sciences* (ed. H. H. Goldstine),195–210. Yorktown Heights, NY:IBM, 1967.

[33] Longuet-Higgins, M.S. and Stewart, R.W. Radiation stresses and mass transport in gravity waves, with applications to "surf beats". *Journal of Fluid Mechanics* **13**, 481–504, 1962.

[34] Longuet-Higgins, M.S. and Stewart, R.W. A note on wave set-up. *Journal of Marine Research* **21**, 4–10, 1963.

[35] Longuet-Higgins, M.S. and Stewart, R.W. Radiation stresses in water waves; a physical discussion, with applications. *Deep Sea Research and Oceanographic Abstracts* **11**, 529–562, 1964.

[36] Lynett, P. J. Nearshore wave modelling with high-order Boussinesq-type equations. *Journal of Waterway, Port, Coastal and Ocean Engineering* **132**, 348–357, 2006.

[37] Ma, G., Shi, F., & Kirby, J. T. Shock-capturing non-hydrostatic model for fully dispersive surface wave processes. *Ocean Model.* **43**, 22–35, 2012.

[38] Madsen, P. A., Sørensen, O. R. & Schäffer, H. A. Surf zone dynamics simulated by a Boussinesq-type model. Part I: model description and cross-shore motion of regular waves. *Coast. Eng.* **32**, 255–287, 1997.

[39] Musumeci, R.E. and Svendsen, I.A. and Veeramony, J. The flow in the surf zone: a fully nonlinear Boussinesq-type of approach. *Coast. Eng.* **52**, 565–598, 2005.

[40] Nwogu, O. Alternative form of Boussinesq equations for nearshore wave propagation. *J. Waterw. Port Coast.* **119**, 618–638, 1993.

[41] Nwogu, O. K. Numerical prediction of breaking waves and currents with a Boussinesq model. In *Coastal Engineering 1996, Proc. 25th Int. Conf.* (ed. Billy L. Edge) **25**, 4807–4820, ASCE, 1996

[42] Peregrine, D. H. Long waves on a beach. *J. Fluid Mech.* **27**, 815–827, 1967.

[43] Pope, S. B. Turbulent Flows. *Cambridge University Press.* Cambridge, 2000.

[44] Richard, G.L. Élaboration d'un modèle d'écoulements turbulents en faible profondeur. Application au ressaut hydraulique et aux trains de rouleaux. PhD thesis, Université d'Aix-Marseille, 2013.

[45] Richard, G. L. and Gavrilyuk, S. L. A new model of roll waves: comparison with Brock's experiments. *J. Fluid Mech.* **698**, 374–405, 2012.

[46] Richard, G. L. and Duran, A. and Fabrèges, B. A new model of shoaling and breaking waves. Part 2. Run-up and two-diemnsional waves. *J. Fluid Mech.* **867**, 146–194, 2019.

[47] Schäffer H.A. and Madsen, P.A. and Deigaard, R. A Boussinesq model for waves breaking in shallow water. *Coastal Engineering* **20**, 185–202, 1993.

[48] Serre, F. Contribution á l'étude des écoulements permanents et variables dans les canaux. *La Houille Blanche* **6**, 830–872, 1953.

[49] Smit, P., Zijelma, M. & Stelling, G.S. Depth-induced wave breaking in a non-hydrostatic, near-shore wave model. *Coastal Engineering.* **76**, 1–16, 2013.

[50] Stelling, G. & Zijlema, M. An accurate and efficient finite-difference algorithm for non-hydrostatic free-surface flow with application to wave propagation. *Int. J. Numer. Meth. Fluids* **43**, 1–23, 2003.

[51] Svendsen, I.A. Wave heights and set-up in a surf zone. *Coastal Engineering* **8(4)**, 303–329, 1984.

[52] Svendsen, I.A. Analysis of surf zone turbulence. *Journal of Geophysical Research: Oceans* **92**, 5115–5124, 1987.

[53] Teshukov, V. M. Gas-dynamics analogy for vortex free-boundary flows. *J. Applied Mechanics and Technical Physics* **48**, 3, 303–309, 2007.

[54] Ting, F. C. K. and Kirby, J. T. Observation of undertow and turbulence in a laboratory surf zone. *Coast. Eng.* **24**, 51–80, 1994.

[55] Ting, F. C. K. and Kirby, J. T. Dynamics of surf-zone turbulence in a strong plunging breaker. *Coast. Eng.* **24**, 177–204, 1995.

[56] Ting, F. C. K. and Kirby, J. T. Dynamics of surf-zone turbulence in a spilling breaker. *Coast. Eng.* **27**, 131–160, 1996.

[57] Tissier, M., Bonneton, P., Marche, F., Chazel, F., Lannes, D. A new approach to handle wave breaking in fully non-linear Boussinesq models. *Coast. Eng.* **67**, 54–66, 2012.

[58] Tonelli, M. & Petti, M. Simulation of wave breaking over complex bathymetries by a Boussinesq model. *J. Hydraul. Res.* **49**, 473–486, 2011.

[59] Veeramony, J. and Svendsen, I. A. The flow in surf-zone waves. *Coast. Eng.* **39**, 93–122, 2000.

[60] Van Dorn, W.G. Set-up and Run-up uin shoaling breakers *Coast. Eng. Proc.* **1(15)**, 41, 1976.

[61] Viviano, A. and Musumeci, R.E. and Foti, E. A nonlinear rotational, quasi-2DH numerical model for spilling wave propagation. *Applied Mathematical Modelling* **39**, 1099–1118, 2015.

[62] Wei, G., Kirby, J. T., Grilli, S. T. & Subramanya, R. A fully nonlinear Boussinesq model for surface waves. Part I: highly nonlinear unsteady waves. *J. Fluid Mech.* **294**, 71–92, 1995.

[63] Zelt, J. A. The run-up of nonbreaking and breaking solitary waves. *Coast. Eng.* **15**, 205–246, 1991.

[64] Zhang, Y., Kennedy, A. B., Donahue, A. S., Westerink, J. J., Panda, N. & Dawson, C. Rotational surf zone modeling for $O(\mu^4)$ Boussinesq-Green-Naghdi systems. *Ocean Model.* **79**, 43–53, 2014.